RSC Advances

PAPER

View Article Online
View Journal | View Issue

Cite this: *RSC Adv.*, 2025, **15**, 33336

Double enhanced piezoelectric wound dressing for nonarticular zones

BeiBei Yang,[a] Sheng Wan,[b] Zhe Chen[b] and Qingjie Liu *[b]

Piezoelectric wound dressings with robust antibacterial properties are essential for preventing infections and promoting healing in low-strain (~5%) non-articular regions, where conventional strain-responsive dressings exhibit limited efficacy. To address this challenge, we developed a self-powered fibrous dressing using polarized poly(vinylidene fluoride) (PVDF) nanofibers incorporating tetragonal barium titanate (BT), leveraging BT's piezoelectric coefficient to boost electromechanical conversion. A homemade dynamic stretching testing device simulated skin deformation and showed that 8% PVDF-BT composites generated 3.1 V under 5% strain-insufficient to produce reactive oxygen species (ROS) eliminating 99% bacteria within 30 minutes while maintaining biocompatibility. The *in vivo* studies revealed exceptional healing performance, achieving 80% wound closure by day 7 and complete regeneration with smooth epidermal tissue by day 12. This study proposes a dual-enhancement strategy—combining material hybridization (PVDF-BT) and optimized polarization—to design strain-adaptive piezoelectric dressings for low-deformation anatomical sites. The optimized PVDF-BT system demonstrates significant potential for self-powered wound management, synergizing electrical stimulation and ROS-mediated antibacterial action to accelerate tissue repair in clinically challenging low-strain non-articular zones.

Received 14th June 2025
Accepted 6th September 2025

DOI: 10.1039/d5ra04222d

rsc.li/rsc-advances

1 Introduction

Chronic wound infections remain a critical healthcare burden, with over 60% of delayed healing cases attributed to persistent bacterial colonization.[1] Traditional antibiotic therapies, while initially effective, face critical limitations due to escalating drug resistance and systemic toxicity risks.[2,3] Furthermore, alternative antibacterial agents, including inorganic nanomaterials (*e.g.*, silver, zinc, and copper) along with organic compounds (including quaternary ammonium salts and alkylated polyethylenimine) have been extensively employed for bacterial eradication.[4,5] This dilemma has driven extensive exploration of alternative antibacterial strategies, particularly those leveraging reactive oxygen species (ROS)-highly oxidative molecules (primarily including hydroxyl radicals ($^{\bullet}OH$), superoxide anions ($^{\bullet}O^{2-}$) and singlet oxygen ($^{1}O_2$)) capable of disrupting bacterial membranes through lipid peroxidation and protein denaturation.[6,7]

Nevertheless, current ROS-mediated antibacterial platforms predominantly rely on external energy inputs, including photodynamic therapy requiring continuous light irradiation and sonodynamic approaches dependent on ultrasound equipment.[8] These modalities present inherent drawbacks: light-based systems suffer from limited tissue penetration depth (mostly <2 mm for the visible spectrum) and potential photothermal damage,[9] while ultrasound-assisted methods lack portability for extended wound care.[10] Moreover, intermittent energy supply in these systems leads to discontinuous ROS generation, compromising bactericidal efficacy.[11]

Besides, electrical stimulation emerges as a promising alternative, with demonstrated capacity to induce ROS bursts through piezoelectric polarization effects.[12] However, conventional electroactive wound dressings require external power sources (typically 3–5 V), creating impractical bulkiness and electrical safety concerns.[13] Recent advances in self-powered systems offer transformative potential by harvesting biomechanical energy from natural motions (*e.g.*, joint flexion, respiratory movement).[14] Triboelectric nanogenerators convert mechanical friction into electricity, yet their operational requirement for sustained mechanical friction (frequency >5 Hz) risks inducing secondary tissue damage at skin wound sites.[15]

Piezoelectric biomaterials present a paradigm-shifting solution by converting ambient mechanical stimuli into localized electric fields, enabling continuous ROS generation without external power.[16] Current material systems face a critical performance-flexibility dichotomy: inorganic piezoelectrics (*e.g.*, $BaTiO_3$, $d_{33} \approx 190$ pC N^{-1}) demonstrate superior charge generation but lack mechanical compliance for epidermal

[a]*College of Music, Leshan Normal University, Leshan 614000, China. E-mail: yangbb1987@sina.com*

[b]*Sichuan Polytechnic University, Deyang 618000, China. E-mail: wansheng@scpu.edu.cn; chenz@scpu.edu.cn; liuqj@my.swjtu.edu.cn*

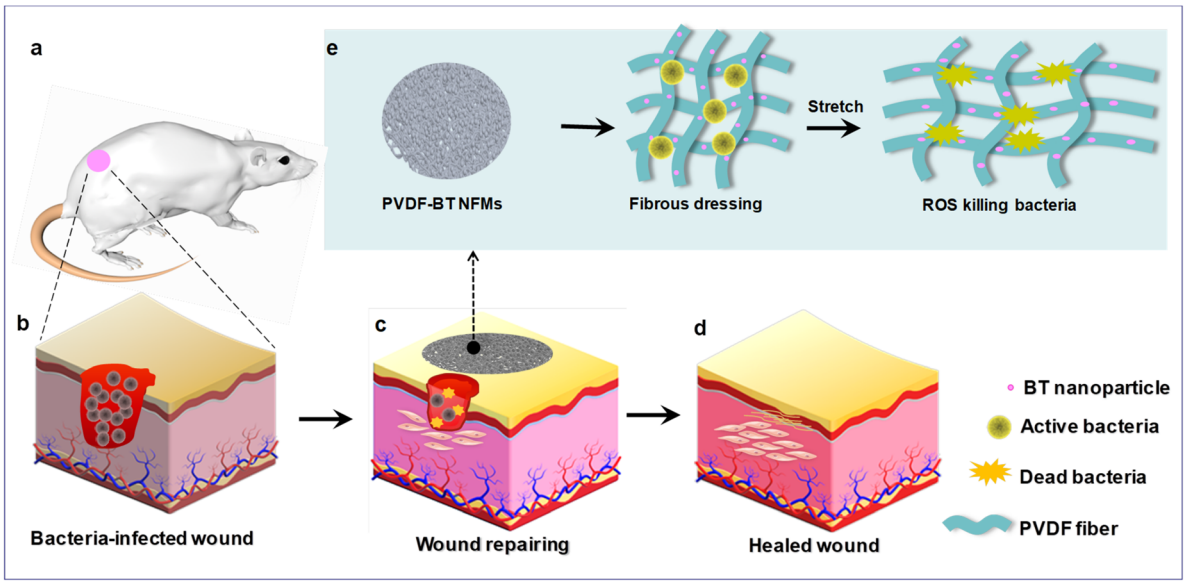

Scheme 1 Schematic illustration of bacterial-killing mechanism with piezoelectric fibrous dressing. (a) Skin wounds occurred on restricted strain sites and (b) accompanied by bacterial infection. (c) Wound repairing progress with PVDF-BT NFMs covered and (d) Skin wound repaired. (e) Bacteria-killing through piezoelectric effects of NFMs.

integration, while flexible organic polymers (*e.g.*, PVDF, $d_{33} \approx 30$ pC N^{-1}) exhibit insufficient piezoelectric response for clinical-grade antibacterial requirements.[17,18] This fundamental limitation underscores the urgent need for hybrid material systems that synergize high piezoelectric coefficients with tissue-adaptive flexibility.[19] Besides, polarization with high electric field could further strengthen the electrical output of piezoelectric materials.[20]

Herein, we present a hierarchically structured nanofibers (NFs) system integrating PVDF fibers with and tetragonal BT (barium titanate) nanoparticles through synergistic electrospinning and polarization with DC (direct current) electric field.[21] Skin wounds occurred on restricted strain sites and always accompanied with bacterial infection (Scheme 1a and b), the nanofiber mats (NFMs) were shaped into wound dressings matching the wound contours and applied to the affected areas (Scheme 1c). These mats could convert biomechanical energy from minor skin deformations induced by bodily movements into piezoelectric voltage (Scheme 1d). To quantitatively assess their piezoelectric response under mechanical stress, a custom dynamic stretching device was developed to simulate *in vivo* skin stretching. *In vitro* and *in vivo* experiments confirmed that the optimized composite demonstrated excellent biocompatibility and efficient ROS generation for antibacterial effects, thereby preventing bacterial infection while accelerating wound healing and tissue regeneration (Scheme 1e). This approach offers a promising pathway for designing self-powered biomaterials with potential applications in wound care.[22]

To tackle these challenges, this study develops a layered piezoelectric dressing that combines precisely engineered inorganic nanoparticles (BT) with electrospun polymeric networks.[23] By optimizing interfacial polarization through crystal phase alignment and surface charge modulation, our design achieves about 5 fold enhancement in piezoelectric output compared to conventional PVDF systems. This bioinspired design achieves breakthrough advancements: A record-high piezoelectric voltage output of 3.1 V under physiologically relevant 5% cyclic strain, surpassing previous reports. Amplified ROS generation through piezoelectric potential-driven oxygen reduction reactions. Systematic investigations combining finite element modeling and *in situ* Kelvin probe force microscopy reveal that the tetragonal BT arrays establish continuous polarization pathways, effectively amplifying interfacial charge separation efficiency. The resultant ROS flux demonstrates broad-spectrum antimicrobial activity (eradication rates > 99% against bacteria within 30 minutes) while maintaining cytocompatibility with fibroblasts. This double-enhanced piezoelectric platform eliminates reliance on external energy sources, offering a paradigm for next generation intelligent wound management. Particularly, this study introduces a new approach for creating strain-responsive self-powered biomaterials, offering significant potential for combating infections in immobilized wound environments.

2 Materials and methods

2.1. Materials

Poly(vinylidene fluoride) (PVDF, Mw = 32 kDa) was obtained from Shanghai Zhaocheng Scientific Development Corp. (Shanghai, China), poly(D,L-lactide) (PDLLA, Mw = 13 kDa) was synthesized through ringopening polymerization of D,L lactic acid using stannous chloride as catalyst.[24] BT was procured from Sigma (St. Louis, MO). All the electrophoresis reagents, and protein molecular weight marker were from Beyotime Institute of Biotechnology (Shanghai, China). *S. aureus* was obtained from the Chinese Medical Culture Collection Center

(Beijing, China), while all other chemicals, unless specified, were analytical-grade reagents sourced from Chang-Zheng Regents Company (Chengdu, China).

2.2. Strain defining of rat skins

The deformations of rat skins caused by breathing and walking in daily life were evaluated by measuring the mechanical deformation of conductive PVDF/CNT fibrous strips. All animal procedures were performed in accordance with the Institutional Guide for the Care and Use of Laboratory Animals of China and approved by the University Animal Care and Use Committee. 6–8 weeks old Male Sprague-Dawley rats (around 160 g) were received from Sichuan Dashuo Biotech (Chengdu, China). Animals were anesthetized by intraperitoneal injection of sodium pentobarbital at a dose of 4 mg kg^{-1} of the body weight, and their dorsal hair was shaved. Three fibrous strips were positioned separately in parallel directions and fixed to back skin (non-articular regions) using polyurethane (PU) films. The location of strains assessed was the same area for the wound healing testing. These strips were connected to copper wires at both ends. The timely resistance fluctuation caused by routine strains was monitored using an electrometer. To establish the strain-resistance curve of composite fibers, the fibrous strips were tested under a series of known strains from 0–15%.[25]

2.3. Preparation of NFMs

PVDF non-woven NFMs were prepared through electrospinning (ES) as mentioned previously.[26] In brief, PVDF solution (30%, w/v) was provided by dissolving PVDF in the mixture of acetone and dimethylformamide (DMF) at a volume ratio of 1/1. Mixed solution of PVDF with different BT proportion in DMF was loaded into the syringe, which was attached to the positive electrode, and pumped with a microinject (Zhejiang University Medical Instrument Company, Hangzhou, China) at feed rate of 12 mL h^{-1}. The ES voltage 15 kV was established at a distance of 15 cm with DC power supply (Tianjing High Voltage Power Supply Company, Tianjing, China) and electric field for ES was 1 kV cm^{-1}. PDLLA fibers was prepared with dichloromethane and DMF (8/2, v/v) through similar ES method. The PVDF and PVDF-BT NFs were collected from an aluminum sheet and be further polarized during 15 kV cm^{-1} DC field for 15 min.

2.4. Characterization of PVDF-BT NFMs

Scanning electron microscope (SEM, FEI Quanta 200, The Netherlands) was used to observe the morphology of all the fibrous mats, and the BT distribution in PVDF NFs was characterized by atomic force microscope (AFM, MultiMode8, USA). The fiber arrangement and average diameter were determined from SEM images by using imaging tools. X-ray diffractometer (XRD; Philips X'Pert PRO, The Netherland) was used to examine the crystal phases of all the fibers.

2.5. Piezoelectric power output of NFMs

The NFMs were sectioned into circular specimens (8 mm diameter) and mounted on a custom built dynamic stretching device using PU film to simulate *in vivo* skin deformation. Conductive resin was used to attach electrodes to the top and bottom surfaces of the NFMs, and the piezoelectric response under strain was measured using an electrometer (Keithley 6514).

2.6. Antibacterial activity *in vitro*

The antibacterial efficiency of PVDF, PVDF-BT and PDLLA fibrous mats was determined against *S. aureus* using the serial method as follows. Briefly, *S. aureus* was inoculated into liquid medium and overnight incubation. The stretching device was used to hold fibrous mats, which were stretched at settled strain and frequency. Nanofiber mats were seeded with 10 μL of *S. aureus* suspensions and at the concentration of 5 × 106 CFU per mL.[27] After shaking at 150 rpm for 18 h at 37 °C. Antibacterial activity of the PVDF-BT could be shown qualitatively as be compared the number of colonies surviving on the plates after the sterilization through PVDF, PVDF-BT and PDLLA NFMs. The antibacterial effects of each NFMs under different strain were determined after incubation of bacteria for different time periods as described previously. Briefly, *S. aureus* suspensions of 20 μL were added into stretching device at 1 × 106 CFU per mL per well, filling with 480 μL of PBS. Bacteria were treated with NFMs for 12 h, the bacterial cells were centrifuged, fixed in 4% glutaraldehyde for 4 h, rinsed with water, and dehydrated through graded ethanol solutions.

2.7. *In vitro* cytotoxicity of NFMs

Systemic toxicity testing of NFMs was performed using a dynamic stretching device set at 5% strain. NIH 3T3 fibroblasts, sourced from the American Type Culture Collection (Rockville, MD), were maintained in DMEM medium (Gibco BRL, Grand Island, NY) supplemented with 10% FBS and 1% penicillin–streptomycin (Sigma, St. Louis, MO). These cells were seeded onto various NFMs within the culture apparatus at a density of 3000 cells per well and allowed to adhere for 12 h. Following cyclic stretching for 2 h, the cells were further incubated for 48 h. Subsequently, the medium in each well was replaced with 100 μL of fresh DMEM containing 5 mg mL^{-1} CCK-8 (Cell Counting Kit-8, Kumamoto, Japan). After 4 h of incubation, absorbance at 450 nm was measured using a microplate reader (Bio-Tek Elx-800, USA).[28]

2.8. ROS generation of NFMs

To assess the ROS production capacity of NFMs, a colorimetric approach utilizing methylene blue oxidation was adopted.[29] Briefly, NFMs were immobilized in the dynamic culture apparatus, and 500 μL of MB-containing PBS (10 mg mL^{-1}) was introduced. Following 60 minutes of cyclic stretching, the solution's absorbance was quantified at 665 nm using UV-Vis spectroscopy.

2.9. Antibacterial activity *in vivo*

The antibacterial ability of PVDF-BT fibrous mats was evaluated on the *S. aureus* infection model. Briefly, equivalent SD mice (as

mentioned above) were received from Sichuan Dashuo Biotech company and all animal procedures were approved by the Leshan Normal University Animal Care and Use Committee (Animal ethics certificate number, L2025019). Following dorsal hair removal, the mice were anesthetized *via* intraperitoneal injection of sodium pentobarbital (40 mg kg^{-1}, body weight). A circular full thickness wound (8 mm in diameter) was surgically induced on the dorsal skin. Subsequently, each wound was inoculated with 10 μL of *S. aureus* suspension (10^6 CFU per mL) and covered with different fibrous mats, gauze and PU film, the mice were monitored for survival for 12 days, and wound images were consistently recorded (he excess hair at the edge of the wound will be shaved off, in order to show wound repairing status).[30] After 3 days of treatment, the wound tissues were collected and homogenized, the diluted samples were spread onto Luria-Bertani agar plates for viable bacterial counting. Following a 12 days treatment period, the skin tissues surrounding the wound sites were collected and fixed in 4% neutral formalin solution for 24 hours at 4 °C. The tissue samples were routinely processed into sections, stained with hematoxylin and eosin (H&E) as well as Masson's trichrome, and subsequently examined under a microscope (Nikon Eclipse E400, Japan).

2.10. Statistical analysis

Results are presented as mean ± standard deviation. For comparisons involving multiple groups, analysis of variance was applied, while differences between two groups were assessed using a two-tailed Student's *t*-test. A *p*-value of less than 0.05 was considered statistically significant.

2.11. Ethics statement

All methods were performed in accordance with relevant guidelines and regulations. The guidelines for animal studies follow the regulations defined by the ARRIVE guidelines (**https://www.arriveguidelines.org**).

3 Results

3.1. Quantification of cutaneous strain dynamics in rodent model

To characterize epidermal strain magnitudes during routine activity, flexible piezoresistive sensors were fabricated *via* electrospinning of PVDF/carbon nanotube (CNT) composites (0.4 × 1.2 mm). Following insulation coating (0.1 mm thickness), the sensors exhibited a linear resistance–strain relationship ($R^2 = 0.98$) up to 15% strain (Fig. 1a).[31] Triplicate sensors were surgically affixed to depilated dorsal regions of anesthetized Sprague-Dawley rats (chloral hydrate, 40 mg kg^{-1}) in orthogonal orientations (Fig. 1b and c). Real-time monitoring during ambulation and grooming revealed peak transient strains of 5.0 ± 0.2% in non-articular regions, with directional analysis confirming isotropic strain distribution (Fig. 1d). This quantification informed subsequent piezoelectric testing parameters to ensure physiological relevance.[32]

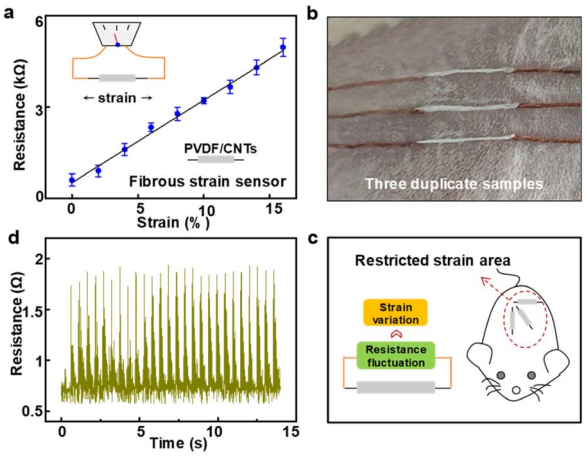

Fig. 1 Strain analysis of the rat skin. (a) Linearly resistance change of the fibrous strips as the strain increased. (b) Three strips stuck on the skin for strain detection. (c) Different directional testing of epidermal strains of rat skin. (d) Variations in the resistance of fibrous strips under normal daily conditions in rats.

3.2. Structural and crystallographic characterization of nanofibers

The electrospun PVDF-BT NFMs exhibited a uniform thickness of approximately 1 mm, with randomly oriented fibers averaging 850 nm in diameter (Fig. 2a). This porous architecture, coupled with inherent flexibility, rendered the membranes highly suitable for wound dressing applications by facilitating gas exchange and efficient absorption of wound exudate.[33] X-ray diffraction (XRD) analysis revealed the crystalline phase composition of the PVDF matrix. A prominent diffraction peak at $2\theta = 20.7°$ (Fig. 2b), corresponding to the (110) crystallographic plane of the piezoelectric β-phase, confirmed successful poling during electrospinning and further polarization. The incorporation of BT nanoparticles was further validated by atomic force microscopy (AFM), which demonstrated homogeneous dispersion of BT particles (50–100 nm) across the PVDF

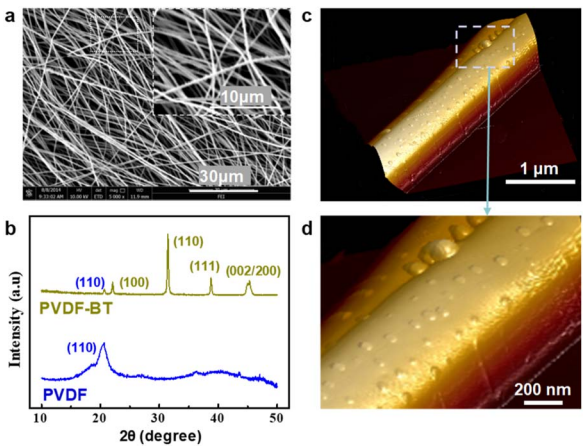

Fig. 2 (a) SEM image of PVDF-BT NFMs. (b) XRD patterns of PVDF and PVDF-BT NFMs. (c) AFM diagram and (d) Partial enlarged view of PVDF-BT NFMs.

fiber surfaces (Fig. 2c and d). The evenly distribution is critical for enhancing interfacial polarization and stress transfer within the composite.[34]

3.3. Development of a biaxial dynamic culture system

A multiaxial strain apparatus was engineered to simulate *in vivo* mechanical loading while enabling simultaneous piezoelectric characterization and bacterial culture, the assembly included a metal cover, two seal rings, a valve-equipped metal holder, along with a plastic support and metal base (Fig. 3a and b). Key components included a pneumatically actuated polydimethylsiloxane (PDMS) membrane (20 μm thickness) integrated with independent culture chambers (Fig. 3c). PVDF-BT NFMs (8 mm diameter, Fig. 3d) were mounted onto the membrane, with cyclic negative pressure (−10 to −80 kPa) inducing programmable biaxial strains (1–15% at 0.5 Hz). Cells or bacteria were seeded on the fibrous mats and the culture media were added in the chamber. Pumping out the internal air created negative pressure across the PU film, with the consequent deformation extending the mats (Fig. 3e). This system permitted real-time assessment of piezoelectric outputs under dynamically strained bacterial cultures, closely mimicking *in vivo* mechanical conditions. Six individual stretching units were connected together with the main channel through their air valves to construct an integrated testing device (Fig. 3f).

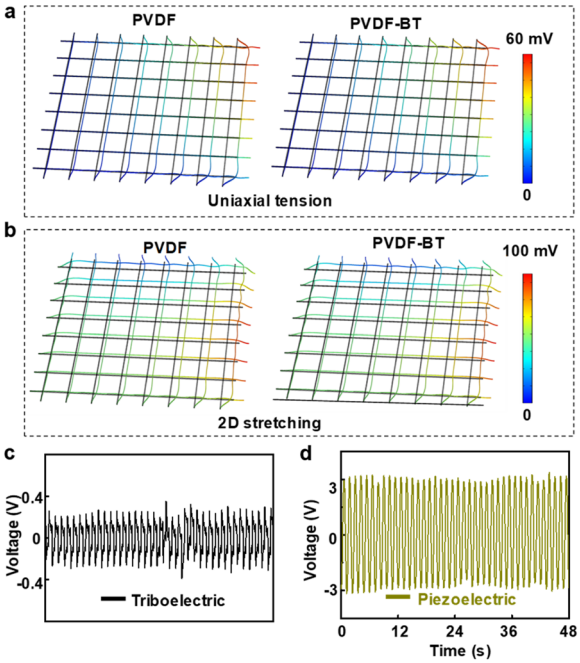

Fig. 4 Piezoelectric output. (a) Simulation of piezoelectric outputs of PVDF and PVDF-BT nanofiber under uniaxial tension and (b) 2D stretching. (c) Triboelectric and (d) Piezoelectric outputs of PVDF-BT NFMs tested with Keithley 6514.

3.4. Piezoelectric performance under simulated physiological loading

First of all, we investigated the piezoelectric outputs of the NFMs using Comsol simulations at the microscope scale. A strain of 5% was imposed on simplified fibrous mesh (850 nm in diameter, 100 μm in length) in two typical conditions (uniaxial or 2D stretching in planes). The measurements showed that applying uniaxial stretching to the fibrous mesh produced roughly 20 mV of piezoelectric voltage in the nanofibers, and a larger piezopotential about 50 mV was induced

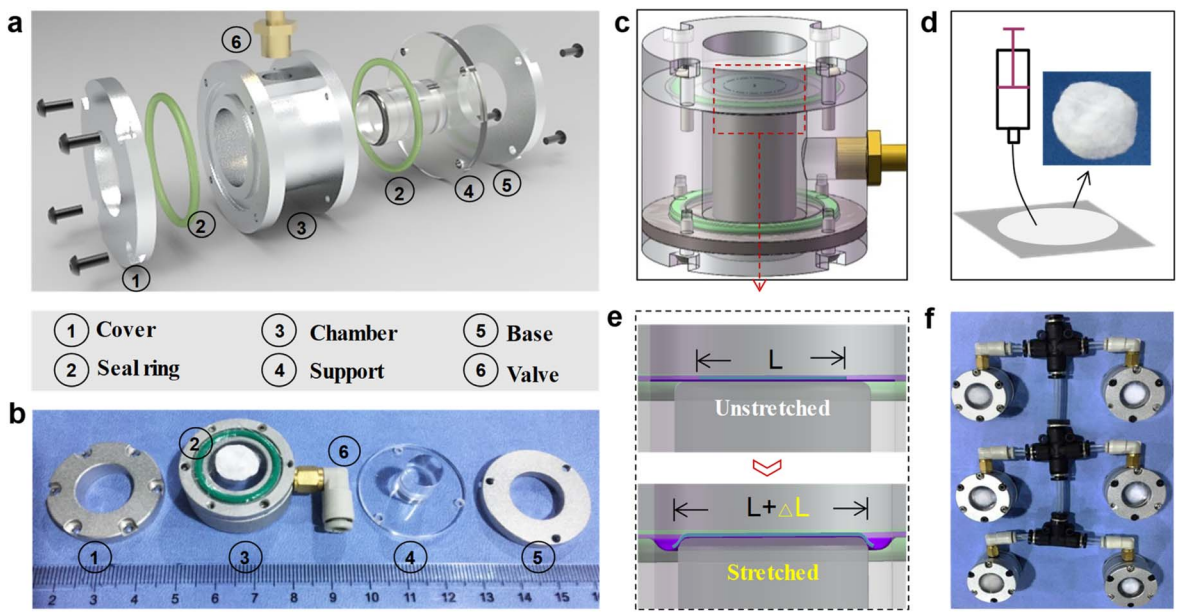

Fig. 3 (a) Dynamic stretching apparatus. (b) Components of stretching apparatus. (c) Assembled stretching unit (d) circular fibrous mat prepared from ES for piezoelectric testing. (e) Schematic illustration of the testing mechanism. (f) Assembled testing device with 6 parallel units.

when the same loads was applied on NFMs, as shown in Fig. 4a. Then orthogonal stretching loaded in plane were applied on fibrous mesh. A significant larger voltage was generated on NFMs (around 90 mV) was produced on the fiber due to significant increased piezoelectric coefficient with addition of BT nanoparticles, as pure PVDF nanofiber could only provide about 40 mV, as shown in Fig. 4b. Meanwhile, single PVDF nanofiber output around 0.4 mV when the length decreased to 1 μm, A similar decreasing trend was observed under tensile strain on NFMs, though with higher voltages (0.9 mV). These results indicate that millivolt-scale voltages at bacterial dimensions could be generated along the fiber, sufficient for ROS production in antibacterial applications. Since triboelectric effects commonly occur when materials of differing electronegativities come into contact,[35] their contribution was assessed by stretching non-piezoelectric PDLLA. The resulting output voltage at 5% strain was approximately 0.27 V (Fig. 4c), substantially lower than the 3.1 V piezoelectric response of PVDF-BT NFMs (Fig. 4d).

3.5. *In vitro* antibacterial properties of NFMs

The dynamic culture system revealed strain-enhanced antibacterial efficacy against *S. aureus*. PVDF-BT NFMs achieved 99% bactericidal efficiency within 30 minutes (Fig. 5a and b), outperforming pure PVDF (around 67%) and PDLLA (<10%). ROS quantification *via* 2′,7′-dichlorodihydrofluorescein diacetate assays demonstrated 50% greater oxidative stress induction by PVDF-BT, PVDF *versus* PDLLA (Fig. 5c). Fig. 5d illustrates the morphological alterations of bacteria on PDLLA and PVDF-BT. In the PDLLA group, *S. aureus* exhibited smooth surfaces. However, following PVDF-BT treatment, wrinkles and pores formed on the bacterial surfaces, likely due to oxidative stress and localized electroporation, which compromised the membrane integrity. Cytotoxicity screening (CCK-8 assay) revealed transient viability reduction in NIH 3T3 fibroblasts during active piezoelectric stimulation (5% strain, 2 h), with almost full recovery to viability after 48 h (Fig. 5d). This biphasic behavior aligns with piezoelectric-mediated electrical stimulation paradigms promoting late-stage proliferation.[36]

3.6. *In vivo* anti-infective and regenerative performance

The antibacterial and wound-healing properties of pure PVDF and PVDF-BT were further evaluated using a *S. aureus* -infected wound model, filled with fibrous mats and covered with gauze, comparing to control group (treated with PDLLA NFs). Fig. 6a exhibited the treating process of skin wound: establishing circle wound, filling with fibrous mats and covered with gauze. As illustrated in Fig. 6b, macroscopic observations over 12 days revealed that the control group exhibited yellow exudate on day 1, whereas PVDF- and PVDF-BT-treated groups showed rapid absorption of the exudate (blue arrows). By day 3, there was no obvious healing phenomenon in wounds in the control group, the PVDF-BT treated groups appeared shrunk significantly. Quantitative analysis (Fig. 6c) demonstrated minimal wound size reduction in the control group after 7

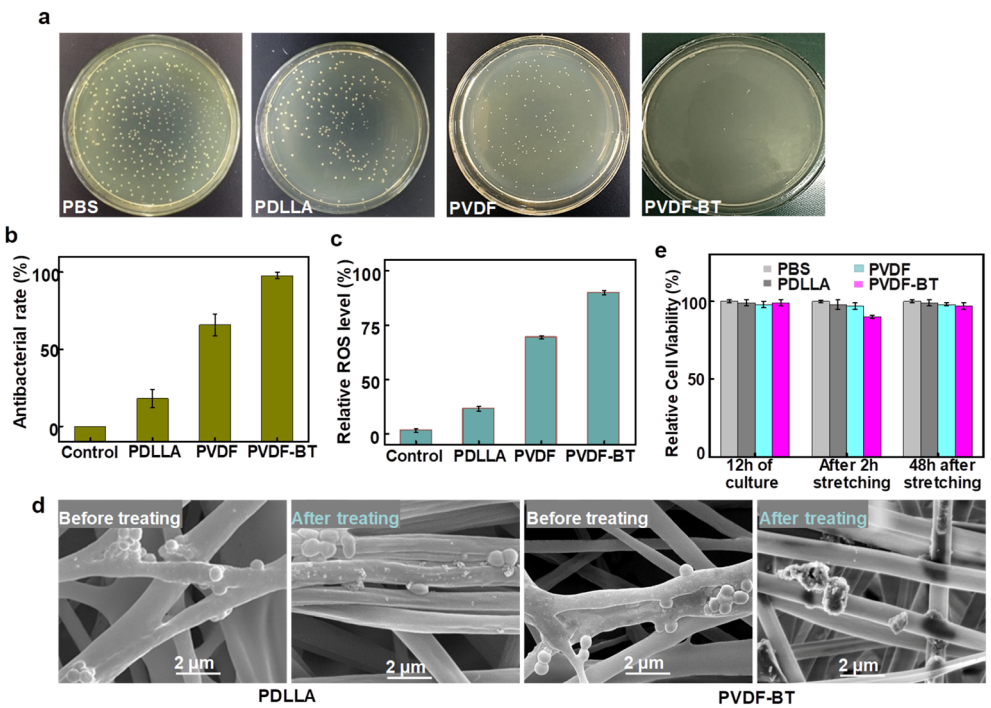

Fig. 5 Characteristic sterilizing effect of NFs. (a) Visual images of agarose plates. (b) Antibacterial rates and (c) relative ROS levels of fibrous mats tested from stretching device. (d) Morphological changes of bacteria on PDLLA and PVDF-BT NFMs. (e) c analysis of various nanofibers to 3T3 cells.

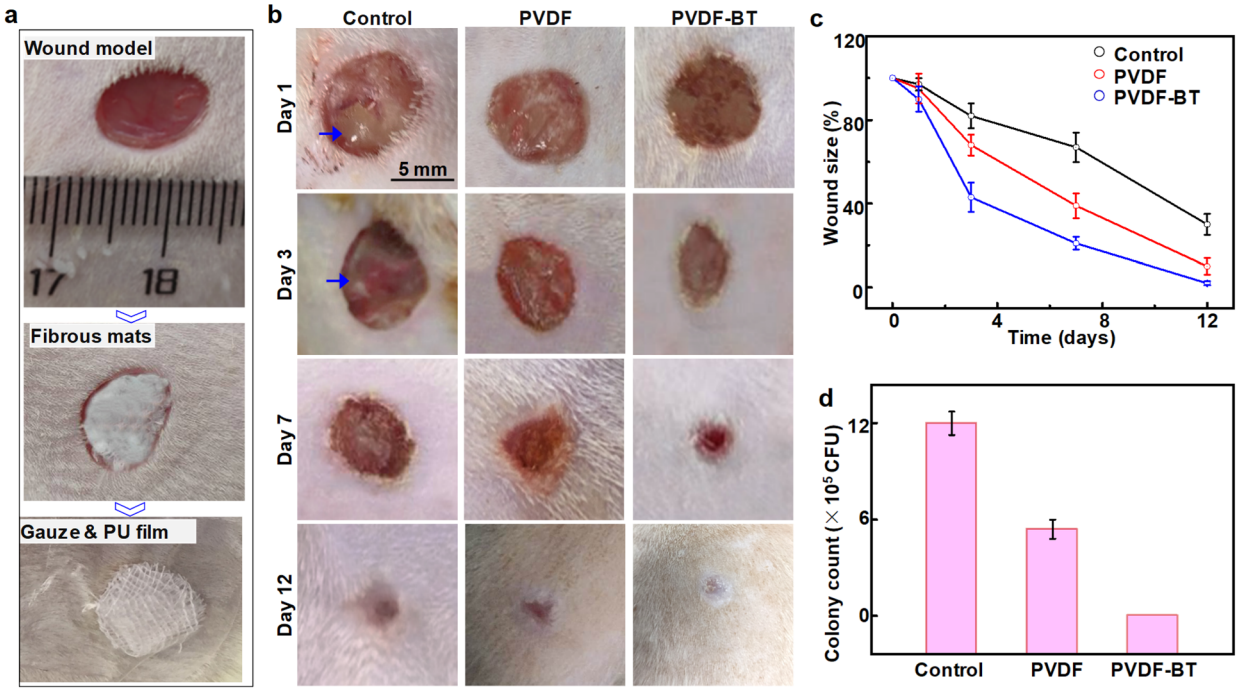

Fig. 6 Wound healing evaluation. (a) Treating process of wound model. (b) Photographs of the wound healing process and (c) wound healing rates after treatment with PDLLA, PVDF and PVDF-BT NFs for 0, 1, 3, 7 and 12 days. (d) Colony counts of the bacteria retrieved from wound areas after culturing for 3 days.

days. In contrast, PVDF-BT-treated groups achieved an 80% healing rate, with near-complete recovery by day 12. Additionally, colony formation assays (Fig. 6d) confirmed the PVDF-BT dressings' strong antibacterial activity, showing complete bacterial eradication in treated wounds within 3 days.

Fig. 7a presents H&E-stained tissue sections from wound regions following 12 days of treatment. The PVDF-BT group exhibited complete skin regeneration, including hair follicles and sebaceous glands. In contrast, control groups showed persistent inflammation (blue arrows) incomplete epidermal tissue, suggesting impaired healing. Additionally, Masson's trichrome staining (Fig. 7b) revealed well-organized collagen fibers (blue) in PVDF-BT treated wounds, resembling healthy skin.[37] By comparison, light blue of the control groups indicated less collagen fibers formed and the PVDF groups revealed disorganized collagen fibers arranged. These findings demonstrate that effective bacterial eradication reduces inflammation and promotes structured tissue repair.

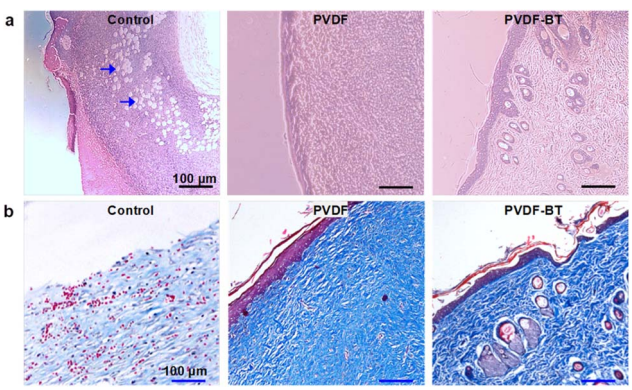

Fig. 7 (a) H&E and (b) Masson's trichrome staining images of tissues around the wound area at 12th day.

4 Discussion

The antibacterial mechanism of the polarized PVDF-BT nanofibers can be attributed to two key effects: (1). Piezoelectric Potential Disruption-Under mechanical strain, the nanofibers generate an extremely high piezoelectric potential, which disrupts bacterial proton chains through charge absorption and impairs mitochondrial energy production, ultimately leading to cell death (Fig. 8a). (2). Oxidative Stress Induction-The localized electric field promotes charge accumulation, inducing harmful oxidative stress through reactive oxygen species (ROS) generation and other cytotoxic effects (Fig. 8b). Due to these dual mechanisms, the PVDF-BT piezoelectric nanofibers exhibit strong antibacterial properties, making them highly suitable for wound dressing applications—particularly in non-articular skin regions where mechanical deformation is frequent (Fig. 8c), and these wounds are common for manual worker, dancers and so on.

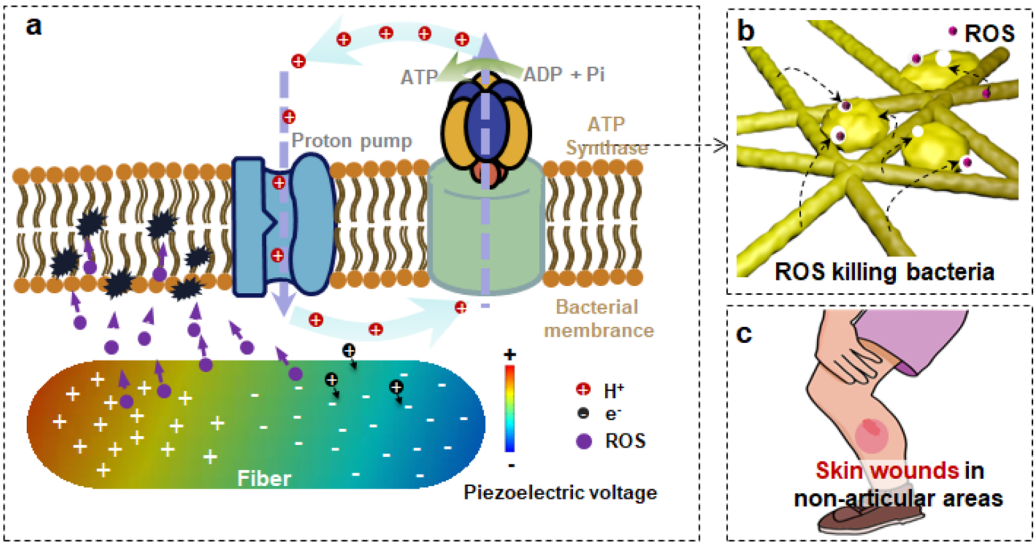

Fig. 8 Enhanced antibacterial dressing for skin wound in non-articular areas. (a and b) Mechanism illustration of piezoelectrical nanofiber to killing bacteria, and suitable for non-articular sites (c).

5 Conclusions

In summary, this study proposes a novel strategy for developing a self-powered, piezoelectric, and antibacterial wound dressing by analyzing skin deformations and the piezoelectric response of carbon nanomaterial composites under physiologically relevant mechanical strain. The findings reveal that polarized PVDF-BT NFMs generate 3.1 V piezoelectric signals when subjected to 5% strain, simulating daily skin stretching. Incorporating 8% BT nanoparticles significantly improves the dielectric properties of fibrous material, increases crystallinity, and amplifies localized stress, thereby enhancing piezoelectric performance.

During the initial treatment phase, the doubly enhanced PVDF-BT NFMs produce sufficient voltage for antibacterial activity. As the composite degrades, its piezoelectric output dynamically diminishes, delivering lower electrical signals conducive to tissue regeneration. Both *in vitro* and *in vivo* experiments confirm the composite's efficacy in generating ROS to eliminate Gram-positive bacteria. These results demonstrate the potential of piezoelectric PVDF-BT NFMs as an efficient antibacterial wound dressing, particularly for dynamic skin areas.

Author contributions

Conceptualization, Beibei Yang, Qingjie Liu, Shen Wan and Zhe Chen; Data curation and formal analysis, Shen Wan and Zhe Chen; Funding acquisition and supervision, Qingjie Liu; Investigation and methodology, validation and writing original draft, Beibei Yang and Shen Wan; Writing review & editing, Qingjie Liu. All authors have read and agreed to the published version of the manuscript.

Conflicts of interest

The authors declare no conflict of interest.

Data availability

All data supporting the findings of this study are included within the manuscript.

Acknowledgements

This work has been supported by the Deyang Science and Technology Program, Sichuan province, China (Grant No. 2024GZ205).

References

1 K. Zegadło, M. Gieroń, P. Żarnowiec, K. Durlik-Popińska, B. Kręcisz, W. Kaca and G. Czerwonka, *Int. J. Mol. Sci.*, 2023, **24**, 1707.
2 A. C. Ewing, N. L. Davis, D. Kayira, M. C. Hosseinipour, C. van der Horst, D. J. Jamieson and A. P. Kourtis, *Emerg. Infect. Dis.*, 2019, **25**, 103–112.
3 W. Bing, Z. Chen, H. Sun, P. Shi, N. Gao, J. Ren and X. Qu, *Nano Res.*, 2015, **8**, 1648–1658.
4 Q. Xu, Z. Zheng, B. Wang, H. Mao and F. Yan, *ACS Appl. Mater. Interfaces*, 2017, **9**, 14656–14664.
5 J. P. Ruparelia, A. K. Chatterjee, S. P. Duttagupta and S. Mukherji, *Acta Biomater.*, 2008, **4**, 707–716.
6 H.-P. Lee, L. Gu, D. J. Mooney, M. E. Levenston and O. Chaudhuri, *Nat. mater.*, 2017, **16**, 1243–1251.
7 J. Tian, H. Feng, L. Yan, M. Yu, H. Ouyang, H. Li, W. Jiang, Y. Jin and G. Zhu, *Nano Energy*, 2017, **36**, 241–249.
8 G. Q. Gu, C. B. Han, J. J. Tian, C. X. Lu, C. He, T. Jiang, L. Zhou and Z. L. Wang, *ACS Appl. Mater. Interfaces*, 2017, **9**, 11882–11888.
9 S. Hao, H. Han, Z. Yang, M. Chen, Y. Jiang, G. Lu, L. Dong, H. Wen, H. Li, J. Liu, L. Wu, Z. Wang and F. Wang, *Nano-Micro Lett.*, 2022, **14**, 107–142.

10 X. Xie, R. Wang, X. Zhang, Y. Ren, T. Du, Y. Ni, H. Yan, L. Zhang, J. Sun, W. Zhang, J. Wang and J. Wang, *Appl. Catal., B*, 2021, **295**, 120315.
11 R. Wang, Q. Liu, A. Gao, N. Tang, Q. Zhang, A. Zhang and D. Cui, *Nanoscale*, 2022, **14**, 12999–13017.
12 M. El-Kaliuoby, M. Amer and N. Shehata, *Polymers*, 2021, **13**, 1869.
13 H. Cao, K. Tang and X. Liu, *Mater. Horiz.*, 2018, **5**, 264–267.
14 J. Qiu, L. Liu, H. Zhu and X. Liu, *Bioact. Mater.*, 2018, **3**, 341–346.
15 C. Tong, L. Li, X. Feng, J. Fan, X. Zhong, X. Liu, B. Liu, Z. Wu and J. Zhou, *Biomater. Sci.*, 2019, **7**, 5097–5111.
16 H. Li, N. Li, Y. Yang, L. Zhang, W. Bai, X. Zhang, Y. Xu and Y. Li, *Nano Energy*, 2023, **115**, 108750.
17 T. Cheng, J. Shao and Z. Wang, *Nat. Rev. Methods Primers*, 2023, **3**, 38.
18 Y. Wei, X. Hu, J. Shao, S. Wang, Y. Zhang, W. Xie, Y. Wu, X. Zeng and L. Zhang, *Mater. Today Commun.*, 2024, **38**, 107715.
19 L. Gazvoda, M. Perišić Nanut, M. Spreitzer and M. Vukomanović, *Biomater. Sci.*, 2022, **10**, 4933–4948.
20 A. M. Khalil, A. H. Hassanin, M. I. El-Kaliuoby, N. Omran, M. Gamal, A. M. El-Khatib, I. Kandas and N. Shehata, *Sci. Rep*, 2022, **12**, 21788.
21 W. Fan, C. Zhang, Y. Liu, S. Wang, K. Dong, Y. Li, F. Wu, J. Liang, C. Wang and Y. Zhang, *Nano Res.*, 2023, **16**, 11612–11620.
22 Z. Wang, M. Xiang, B. Huo, J. Wang, L. Yang, W. Ma, J. Qi, Y. Wang, Z. Zhu and F. Meng, *Nano Energy*, 2023, **107**, 108162.
23 Q. Liu, L. Liu, D. Fan, S. Xie, C. Wang, X. Gou and X. Li, *Appl. Mater. Today*, 2024, **37**, 102120.
24 C. Shanmugam, V. Marimuthu and N. Rajendiran, *React. Funct. Polym.*, 2024, **194**, 105772.
25 Q. Liu, L. Jin, P. Zhang, B. Zhang, Y. Li, S. Xie and X. Li, *ACS Appl. Mater. Interfaces*, 2021, **13**, 10623–10631.
26 X. Liu, J. Tong, J. Wang, S. Lu, D. Yang, H. Li, C. Liu and Y. Song, *J. Mater. Chem. C*, 2023, **11**, 4614–4622.
27 M. Chen, S. Xie, J. Wei, X. Song, Z. Ding and X. Li, *ACS Appl. Mater. Interfaces*, 2018, **10**, 36814–36823.
28 J. M. M. Mohamed, A. Alqahtani, A. Fatease, T. Alqahtani, B. A. Khan, B. Ashmitha and R. Vijaya, *Pharmaceuticals*, 2021, **14**, 781.
29 X. Meng, L. Chen, R. Lv, M. Liu, N. He and Z. Wang, *J. Mater. Chem. B*, 2020, **8**, 2177–2188.
30 M. Chen, J. Wei, S. Xie, X. Tao, Z. Zhang, P. Ran and X. Li, *Nanoscale*, 2019, **11**, 1410–1422.
31 Q. Liu, Q. Wu, S. Xie, L. Zhao, Z. Chen, Z. Ding and X. Li, *Nanotechnology*, 2019, **30**, 375301.
32 X. Pan, Z. Wang, Z. Cao, S. Zhang, Y. He, Y. Zhang, K. Chen, Y. Hu and H. Gu, *Smart Mater. Struct.*, 2016, **25**, 105010.
33 Z. Chen, X. Du, Y. Liu, Y. Ju, S. Song and L. Dong, *J. Mater. Chem. A*, 2018, **6**, 15191–15199.
34 A. Sun, G. Farrell, Y. Semenova, B. Chen, G. Li and Z. Lin, *Optik*, 2011, **122**, 1779–1781.
35 Q. Zheng, B. Shi, Z. Li and Z. Wang, *Adv. Sci.*, 2017, **4**, 1700029.
36 G. Murillo, A. Blanquer, C. Vargas-Estevez, L. Barrios, E. Ibáñez, C. Nogués and J. Esteve, *Adv. Mater.*, 2017, **29**, 1605048.
37 X. Yu, S. Wang, X. Zhang, A. Qi, X. Qiao, Z. Liu, L. Li and Z. Wang, *Nano Energy*, 2018, **46**, 29–38.